Sensors and Materials, Vol. 37, No. 12 (2025) 5609–5623
MYU Tokyo

S & M 4267

Chemical Formula Analysis of High-elasticity Alloys Using Short-range-ordered Structure Model

Hai-Lian Hong,[1,2] Chi-Hsin Yang,[1*] and Hui-Xian Yan[1]

[1]School of Mechanical and Electric Engineering, Sanming University,
Sanming City 365004, Fujian Province, China
[2]School of Navigation, Xiamen Ocean Vocational College, Xiamen 361012, China

(Received June 5, 2025; accepted December 8, 2025)

Keywords: high-elasticity alloy, Friedel spherical periodic oscillation (FSPO), short-range-ordered parameter, chemical formula analysis of alloys

The Friedel spherical period oscillation (FSPO) phenomenon caused by electron density scattering from impurity atoms is investigated in this work using high-elasticity copper alloy as an example. First, in accordance with the theory behind this phenomenon, the range of the smallest electrical neutrality scale that stabilizes in the based alloy is established when impurities are present. Next, this range is contrasted with the face-centered cubic (FCC) solid solution's lattice point locations. The adsorption atomic radius is considered to determine the truncation radius of FSPO and to further determine the shielding range of the electron wave of impurity atoms. In this study, we determine the chemical formula of neighboring and secondary neighboring atoms in the FCC solid solution alloy using the Cowley parameters of two neighboring shells of the alloy, which were obtained using X-ray and neutron diffraction equipment. With A, B, and C standing for the various atom types in the alloy and the number of secondary adjacent atoms x = 2 or 3, the formula can be broadly written as $[AB_{12}]Cx$. The analytical approach described in this work can also be applied to examine other multicomponent high-elasticity alloys, including those found in the Monel series. The results of this study show that various industrial grades of highly elastic alloys can have their chemical formulas determined more easily by theoretically analyzing the relationship between alloy composition and properties from the viewpoint of the nearest-neighbor local electronic structure. This method provides a solid theoretical direction for both the creation of new alloys and the enhancement of performance in already existing alloys. In addition, the analytical framework introduced in this work can be further applied to the innovative design of high-elasticity alloys exhibiting enhanced physical characteristics, thus assisting sensor technology researchers in refining manufacturing processes and facilitating the creation of sensors with improved functionality.

---

*Corresponding author: e-mail: 20190207@fjsmu.edu.cn
https://doi.org/10.18494/SAM5784

1. Introduction

Alloys with high elasticity, recognized for their superior elastic modulus and elastic limit, are crucial in a wide range of electronic components, particularly those applied in aerospace technology, precision instruments, and measurement devices. As an example, the beryllium copper (Cu–2.8Be) alloy is vital for constructing the cathode in high-performance photomultiplier tubes.(1) Another significant material is phosphor bronze, which is commonly used in the production of high-performance wear-resistant parts and elastic components, including bearing materials and electrical connectors.(2) Moreover, owing to its economic advantages, 304 stainless steel is frequently chosen as an elastic material for general-purpose instruments and meters.(3) With the rapid advancement of science and technology, the demands on the performance of high-elasticity alloys have been steadily increasing. Beryllium copper alloys exhibit inadequate stress relaxation resistance at elevated temperatures,(1) while phosphor bronze demonstrates low corrosion resistance under high-temperature conditions.(2) Additionally, spring steels such as 304 stainless steel exhibit relatively low wear resistance and limited tolerance to strong acids and alkalis.(3) As a result, the need to develop alternative systems of conductive elastic alloy materials has become increasingly pressing.

An overview of recent advancements in high-elasticity alloy materials for sensor applications is addressed. Ren *et al.*(4) investigated the annealing behavior of a Ni80Cr20 alloy layer on a 304 stainless-steel substrate, intended for use as a sensing element in thin-film sensors within nitrogen-controlled environments. Owing to the low electrical resistance of nickel–chromium-based alloys, these sensors are capable of detecting minute deformations, resulting in enhanced precision and sensitivity in strain measurements. In Ref. 5, the fabrication of a pressure sensor using a high-elasticity beryllium bronze alloy was discussed, supported by theoretical analysis and simulations that confirm its effective sensitivity response and temperature compensation capabilities. The excellent elasticity of the beryllium bronze enables precise detection within narrow measurement ranges.

In Ref. 6, the systematic optimization of copper–nickel–iron high-elasticity alloys to produce a new material suitable for fluxgate sensor cores was described, presenting an alternative to traditional molybdenum–nickel–iron alloys. This optimized alloy was indicated to provide improved magnetic permeability, leading to increased signal stability and reduced energy requirements compared with standard molybdenum-containing devices. High-elasticity materials are gaining recognition as promising candidates for advanced sensor technologies.

Elastic alloys, such as Cu–Ni–Sn and Ni36CrTiAl, have attracted significant attention because of their outstanding characteristics and adaptability to various environments. However, in Cu–Ni–Sn alloys, a high tin concentration often leads to segregation and the formation of precipitates during alloying.(7) These phenomena enhance electron wave scattering, which significantly reduces electrical conductivity. In Ni36CrTiAl alloys,(8) the quenching process enhances the precipitation of the reinforcing phase Ni3(TiAl), but results in an uneven spatial distribution, negatively affecting the alloy's resistance to corrosion. Moreover, owing to the scarcity of additional alloying components, the formation of Cottrell atmospheres (9) is hindered, which weakens the immobilization of dislocations and consequently reduces the effectiveness of strengthening mechanisms.

The critical factor in developing high-elasticity alloys is the stringent control of their chemical composition and impurity content. In prior studies, alloy compositions were predominantly determined through extensive trial-and-error experiments. This approach has resulted in significant challenges, such as time-consuming processes, high costs, and low efficiency in the development of high-elasticity alloys. To reduce research and development expenses for high-elasticity alloys and shorten their development cycle, it is urgently necessary to establish a theoretical model that can effectively guide the compositional design of these alloys. For a highly elastic alloy, its exceptional physical properties can be attributed to its extremely stable atomic structure. As a result, the main contribution of this study is that we focus on investigating the connection between the properties of alloys and their composition and structure from the perspective of the short-range ordered (SRO) structure in alloys, thus presenting a new method for the design and development of high-performance, highly elastic alloys. Moreover, the novel development of high-performance, highly elastic alloys provides significant assistance to researchers in the sensor domain, promoting improvements in manufacturing processes and supporting the creation of sensors with superior functionality.

The microstructure of copper alloys primarily consists of the γ phase, which features a face-centered cubic (FCC) structure and acts as the high-temperature stable phase of the alloy. The alloy's strength is enhanced while its toughness and ductility are improved through mechanisms such as dislocation locking caused by lattice volume mismatch and elastic strain mismatch pairs, or via the dispersed distribution of second-phase particles that impede dislocation motion within the alloy.(9,10) The properties of the alloys are predominantly determined by the interactions between atoms in the high-temperature stable phase. Nevertheless, under the current experimental conditions, directly obtaining an intuitive understanding of the atomic structure of the high-temperature stable phase remains challenging.

Material macroscopic properties are primarily affected by their stable SRO structures. Extensive research has focused on improving the overall mechanical characteristics of alloys by adjusting these SRO structures.(11,12) This field has been particularly well studied in copper-based alloys. For example, Moody *et al.*(13) demonstrated, through atomic probe tomography experiments and first-principles calculations, that enhancing the short-range ordering of Ag atoms increases the hardness of Al–Ag–Cu alloys. In Ref. 14, Sun *et al.* emphasized that cyclic plastic deformation techniques can elevate both the quantity density and volume fraction of SRO structures, thereby strengthening the tensile properties of Al–Cu–Mg alloys via increased structural density. Chen *et al.*(15) showed that optimizing the casting process promotes the formation of Fe-rich SRO structures, which enhances the strength and ductility of Cu–Sn–Zn alloys. In Ref. 16, Zhao and Liu reported that under diverse aging conditions, Cu–Mg SRO structures significantly improve alloy fatigue resistance. In addition, in this study, we investigate the relationships between other alloy properties, such as corrosion resistance, thermal expansion coefficients, and magnetization intensities, and SRO structures. These advancements have greatly propelled the understanding of the interplay between alloy properties and SRO structures.

The atomic model for alloys presented in Ref. 17 has been utilized across several alloy systems, yielding chemical composition expressions that align well with recognized alloy designations. Nevertheless, the model's formulation originates from the structural features of amorphous alloy atoms, making it inherently empirical. The nonperiodic arrangement observed in amorphous materials is contrasted significantly with the regular, repeating lattice patterns characteristic of solid solutions. Consequently, when this model is employed in the analysis of FCC solid solution alloys, inaccuracies may arise because of structural mismatch.

The main contribution and novelty of our study are grounded in the FSPO phenomenon, and we systematically analyze the atomic shell configuration in the FCC solid solution by leveraging the periodicity of atomic arrangements. Through the derived analytical expression for the chemical composition of the high-elastic alloy, a unique feature associated with the second-shell atoms is identified. Notably, the atomic model for alloys described in Ref. 17 fails to reproduce this outcome.

We used the highly elastic copper alloy as an example and employed an FCC lattice structure to analyze its compositional characteristics. First, by investigating the electronic interaction mechanism between solute and solvent atoms in the highly elastic copper alloy, the range of solute impurities shielded within the FCC solid solution is determined. Subsequently, this range is compared with the lattice positions of the FCC solid solution to identify the central atoms of the two nearest-neighbor clusters. On the basis of the obtained results, the optimal first and second nearest-neighbor structural models of the FCC solid solution are selected. Finally, using the Cowley parameters of the two neighboring shells obtained from X-ray and neutron diffraction experiments, the chemical composition formulas for the atomic structures of both the nearest-neighbor and next-nearest-neighbor atoms in the FCC solid solution alloy are further calculated.

The composition of thirteen types of high-elasticity alloys was analyzed using our proposed method. The results indicate that the atomic chemical structure composition formula of the alloy presented herein is applicable to various mature industrial-grade high-elasticity alloys. In the derived chemical formula, the number of atoms in the second-shell layer is either 2 or 3, and the amount of each element is predominantly an integer. This approach further facilitates the understanding of the relationship between alloy properties and composition from the perspective of the local neighboring electronic structure.

2. Distribution of Atoms in Friedel Spherical Period Oscillation

In materials, electrons and holes function as charge carriers.(18) Within metallic substances, conductive electrons primarily act as the main charge carriers. The extent to which electrons are localized within a material, which indicates their capacity to traverse through it, results in localized interactions. Although electrons are affected by their surrounding conditions, they exhibit relatively unrestricted movement in delocalized areas. These localized electron fluctuations are generally triggered by interactions involving impurities or defects. Impurity scattering induces electron density fluctuations that display quantum mechanical interference patterns, referred to as Friedel spherical periodic oscillations (FSPOs).(19) The experimental evidence of this phenomenon has been documented in multiple systems, such as graphene,(20,21) copper,(22) and hydrogen-intercalated quasi-independent bilayer graphene (hQBG) devices constructed on 6H-SiC (0001) substrates.(22)

Scanning tunneling microscopy (STM) was utilized to detect the interference patterns of FSPO within the local density of states (LDOS) in few-layer graphene.(20,21) These patterns are mainly affected by intra- and intervalley scattering mechanisms on the Fermi surface,(16) which result from Coulombic interactions occurring both within and between hexagonal quantum bilayer graphene (hQBG) layers. Crommie *et al.*(22) used STM to observe concentric ring-shaped standing wave patterns of LDOS that emerge around point defects on the close-packed surfaces of copper (Cu) at low temperatures ranging from 4 to 77 K. At low temperatures, scattering in hQBG is primarily controlled by charged impurities and electron–electron interactions.(23) Through STM experiments, it was determined that these charged impurities stem from hydrogen vacancies situated beneath the hQBG layer, impacting only the Fermi level directly above the defect locations. The fluctuations in LDOS caused by electron-scattering interactions have substantial effects on electronic properties such as electrical conductivity, elasticity, and magnetism. These effects are attributed to alterations in topological characteristics induced by the oscillations. More specifically, when the peaks of the atomic distribution function correspond one-to-one with the troughs of the effective potential energy function for electrons, the Fermi band energy achieves its lowest value, leading to the most stable configuration. The development of novel high-elasticity alloys fundamentally depends on identifying the dimensions of the FSPO within the alloy model and pinpointing its location at the stable resonance position associated with the FSPO.

Because of the local perturbation resulting from the potential energy $\Phi(\vec{r})$ induced by impurity electric ions, an electron having mass m will undergo scattering in a periodic lattice structure. The Schrödinger equation, which is time-independent and corresponds to these scattered electrons, can be formulated as (19)

$$(-\hbar^2/2m)\nabla^2\psi(\vec{r}) + \Phi(\vec{r})\psi(\vec{r}) = E\psi(\vec{r}), \tag{1}$$

where $\hbar$ is the normalized Planck's constant, $(-\hbar^2/2m)\nabla^2$ denotes the kinetic energy operator, $\psi(\vec{r})$ corresponds to the wave function of the electron, and E signifies the total energy of the electron.

Once the wave function $\psi(\vec{r})$ in Eq. (1) is solved, the corresponding probability density function $|\psi(\vec{r})|^2$, which represents the probability of detecting an electron at a specific position vector $\vec{r}$ within a unit volume, can be derived. This quantity provides insight into how electrons are spatially distributed and illustrates the inherent probabilistic behavior of electron localization. As a result, Eq. (1) captures the quantum mechanical state of electrons in a lattice structure and contains detailed information about their spatial probability distribution. According to Häussler,(19) Friedel proposed that the perturbation potential energy function $\Phi(\vec{r})$ for an electron located at the center of an impurity particle and at a distance r from the impurity's position exhibits the relationship shown below.

Equation (1) presents a detailed mathematical representation of the quantum state of an electron in a lattice structure, including elements such as its positional probability distribution. As indicated in the Friedel's result,(19) the perturbation potential energy function $\Phi(\vec{r})$ for an electron positioned at the center of an impurity particle and at a radial distance r from the impurity can be depicted as

$$\Phi(\vec{r}) \propto \cos(2k_F \cdot r + \Theta) / r^3 . \tag{2}$$

Among the defined parameters, k_F indicates the Fermi wave vector and Θ represents the phase offset. The electron density can be determined using the electron perturbation potential energy function by

$$\rho(\vec{r}) = \rho_0 + \delta_n \cos(2k_F \left|\vec{r}\right| + \delta) \Big/ \left|\vec{r}\right|^3 . \tag{3}$$

In this scenario, ρ_0 represents the electron density when in a stable condition. δ_n denotes the amplitude of modulation for electron density, highlighting the level of variation close to impurities. Such amplitude is shaped by the characteristics of the impurities and the interaction mechanism between electrons and impurities. δ signifies the phase factor that affects the spatial arrangement of electron density fluctuations. Varied phase factors result in distinct spatial structures and initiation points of these fluctuations.

From the standpoint of energy, the trough of perturbation potential energy $\Phi(\vec{r})$ corresponds to the region where the external additional potential energy perceived by electrons is relatively minimal. In the context of chemical bond formation, the interaction potential energy between atoms can be regarded as the additional potential energy experienced by electrons owing to external effects. The region with the lowest additional potential energy for electrons corresponds to the region with the lowest interaction potential energy between atoms. This, in turn, corresponds to the region where the overall system energy reaches its minimum. According to the principle of minimum energy,(19) this region is the most stable, and the system tends to favor this energy state. Consequently, within the framework of FSPO, atoms are more likely to reside at the troughs of perturbation potential energy $\Phi(\vec{r})$. Likewise, the probability of electrons being located at the troughs of the potential energy function is higher, resulting in a greater amplitude of the electron wave function at these positions.

From the relationship between the wave function and electron density, where the square of the wave function's amplitude represents the probability density of electron presence, it can be inferred that electron density is higher at the troughs of the potential energy function. During chemical bond formation, atomic orbitals in regions with elevated electron density are more prone to overlap, thereby forming stronger covalent bonds. This enhances the attractive force between atomic nuclei, stabilizing the chemical bonds. Consequently, a higher electron density provides atoms with a more stable electronic environment, encouraging them to reside in these positions.

From the potential energy function $\Phi(\vec{r})$ described in Eq. (2), one can infer that the minimum point is located at positions $2k_F r + \Theta = (2n+1)\pi$. For amorphous alloys, the phase angle $\Theta = \pi/2$ is generally utilized, which facilitates identifying the locations of the trough.

$$r_n = (n + 1/4)\lambda_{F_r}, \quad n = 1, 2, 3\cdots \tag{4}$$

Here, λ_{Fr} denotes the Friedel wavelength, and the different values of n are associated with the trough locations in separate periods.

3. Determination of Number of Nearest-neighbor Atomic Shells

Upon incorporating various alloying elements into solid solution alloys, the imbalance between the total positive charge of positively charged impurity ions and the total negative charge of negatively charged electrons can result in alloy instability, such as phase separation, chemical reactions, or alterations in electrical conductivity. Consequently, maintaining charge balance is essential for ensuring both the structural stability and electrical conductivity of alloys. The magnitude of the Fermi wave vector k_F serves as a critical parameter characterizing specific electronic properties and significantly affects various physical properties, including thermal and electrical conductivities.

By utilizing the equation for a three-dimensional free electron gas described by(24)

$$k_F = (3\pi^2 n)^{1/3}, \tag{5}$$

where n denotes the electron concentration, the Fermi wave vector k_F correlates directly with the cube root of the electron count per unit volume in the substance.

For example, copper exhibits the FCC crystal structure and features a lattice constant indicated by a = 0.361 nm, four atoms per unit cell symbolized as N = 4, and an atomic density described by $n_{atom} = N/a^3$. Since copper is a monovalent metal, where each copper atom provides one free electron, the electron density matches the atomic density.

$$n = n_{atom} = 4/0.361 \times 10^{-9} \approx 8.49 \times 10^{28}\ \mathrm{m}^{-3} \tag{6}$$

Substituting Eq. (6) into Eq. (5), we derive

$$k_F = (3\pi^2 \times 8.49 \times 10^{28})^{1/3} \approx 1.36 \times 10^{10}\ \mathrm{m}^{-1}\ . \tag{7}$$

By substituting the obtained Fermi wave vector k_F to Eq. (5), the functional dependence of the perturbation potential energy on the radial position can be derived.

$$\Phi(\vec{r}) \propto \cos(2.72r + 1.571) / r^3 \tag{8}$$

Equation (8) reveals that the electrons located at position *r* relative to the impurity particle display oscillatory characteristics. Utilizing Eq. (8), the distribution of potential energy in the localized electronic environments of FSPO and adsorbing atoms in the copper alloy, along with the perturbation potential energy function of the material, was numerically determined and graphically represented using MATLAB, as displayed in Figs. 1 and 2. The oscillatory patterns corresponding to two impurity particles are illustrated in Fig. 1, whereas Fig. 2 provides a representation of the spatial arrangement of the FSPO. These simulation results will serve as the basis for further computational analysis in the following stages.

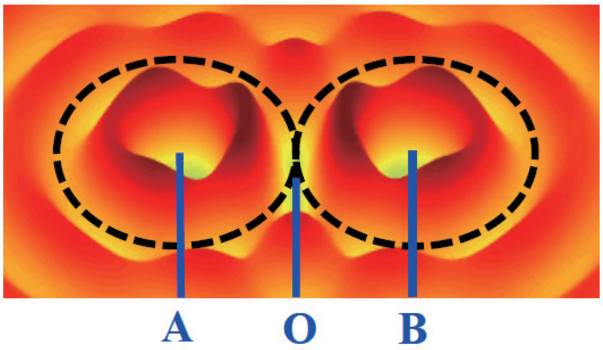

Fig. 1. (Color online) Distribution of potential energy for FSPO and electrons in absorbed atoms.

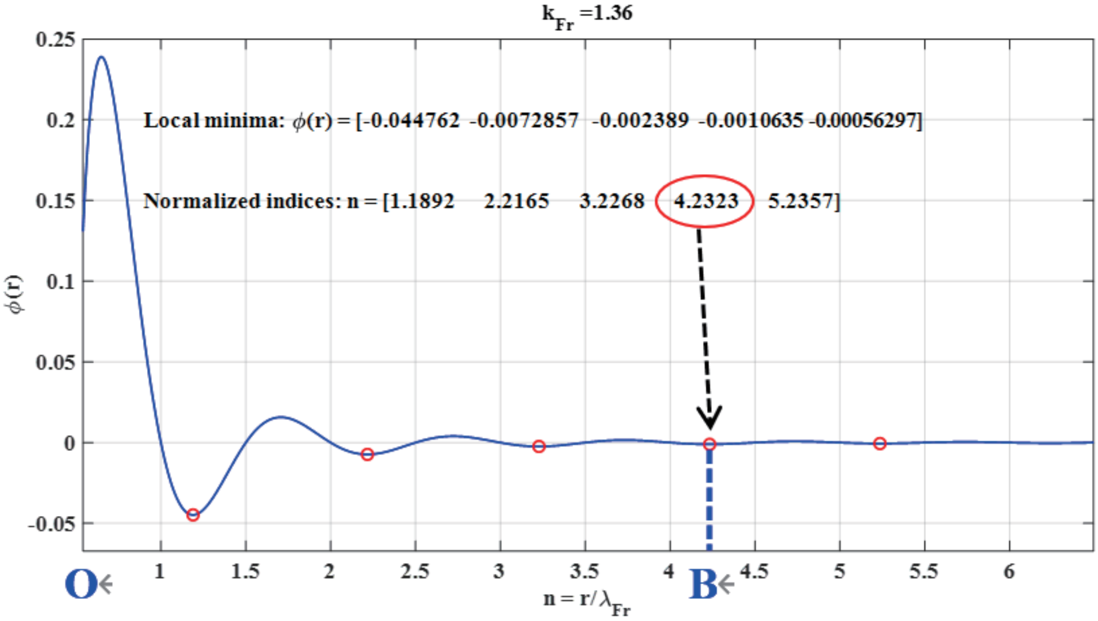

Fig. 2. (Color online) Normalized perturbation potential energy function curve for copper alloy.

According to Ref. 25, the first peak in the interatomic spacing distribution of adsorbed atoms, measured by STM in real copper alloy specimens, is located at 21 nm. The corresponding oscillation loop radius associated with the LDOS at this separation distance is 1.05 nm.

In Fig. 1, A and B represent two adsorbed atoms. The electron waves surrounding these adsorbed atoms interfere with each other, leading to the formation of standing waves. The first nodes of these standing waves are located along circles centered at A and B with radii OA and OB, respectively. Simulation results indicate that the dark ring observed by STM corresponds to the region centered at point O, consistent with the findings reported in Ref. 25. From a physical standpoint, at location O, the presence of impurities does not significantly perturb the potential field distribution within the alloy, which is composed of copper atoms. Consequently, the Friedel oscillation amplitude is substantially suppressed, resulting in an electron density comparable to that of pure copper atoms in the absence of impurity ions.

Substituting Eq. (7) into Eq. (5), we derive λ_{Fr} = 0.231 nm. In our prior research,(26) we demonstrated that the radius for truncating the interference of impurities is

$$r_{cut} = (r_4 + r_5)\lambda_{F_r}/2 = (4.2323 + 5.2357)\lambda_{F_r}/2 = 4.734\lambda_{F_r} = 1.09\,\text{nm}\,\cdot \tag{9}$$

The location derived from Eq. (9) is in exact agreement with the position of the first peak of adsorbed atoms shown in Fig. 2, where the index equals 4.2323 relative to the center of the first dark ring. This further corroborates that at r = 1.05 nm, when the electron wave encounters local potential perturbations induced by impurity atoms, the scattering amplitude in the LDOS of electrons is enhanced by the initial interference occurring at the crest position. Specifically, this corresponds to the dotted circles with radii OA and OB in Fig. 1, which subsequently converge toward the central position O of the first dark ring. The position O of the dark ring corresponds to the destructive interference of the electron wave. At the center O of the dark ring, the LDOS significantly decreases, approaching the LDOS value of substrate atoms. These findings are largely consistent with the conclusion that the probability density of FSPO electrons reaches 1.08 nm at the r_{cut} position near the substrate density, and the position of the first dark ring where the LDOS of alloy matrix atoms markedly diminishes is located at 1.05 nm. In Ref. 27, it is noted that the first position at which Cu-adsorbed Co atoms decrease to the level of background noise occurs between 1.5 and 2 nm, a finding that broadly supports the results presented herein. Equation (9) delineates the minimum scale range of electrical neutrality that tends to stabilize locally within a copper alloy, including contributions from impurity atoms.

4. High-elasticity Alloy Cluster Model

Reference 28 presents a variety of alloy cluster models, with the 1-2 and 1-3 models depicted in Fig. 3. In particular, the 1-2 model features a coordination number of 12 for the nearest-neighbor clusters centered on alloy cluster M, consisting of four central atoms in cluster P_1 and eight central atoms in cluster Q_1. Conversely, the 1-3 model has a higher coordination number of 14, which includes eight central atoms in cluster P_2 and six central atoms in cluster Q_2. As illustrated in Fig. 3(b), the supercluster distribution map indicates that the arrangement of

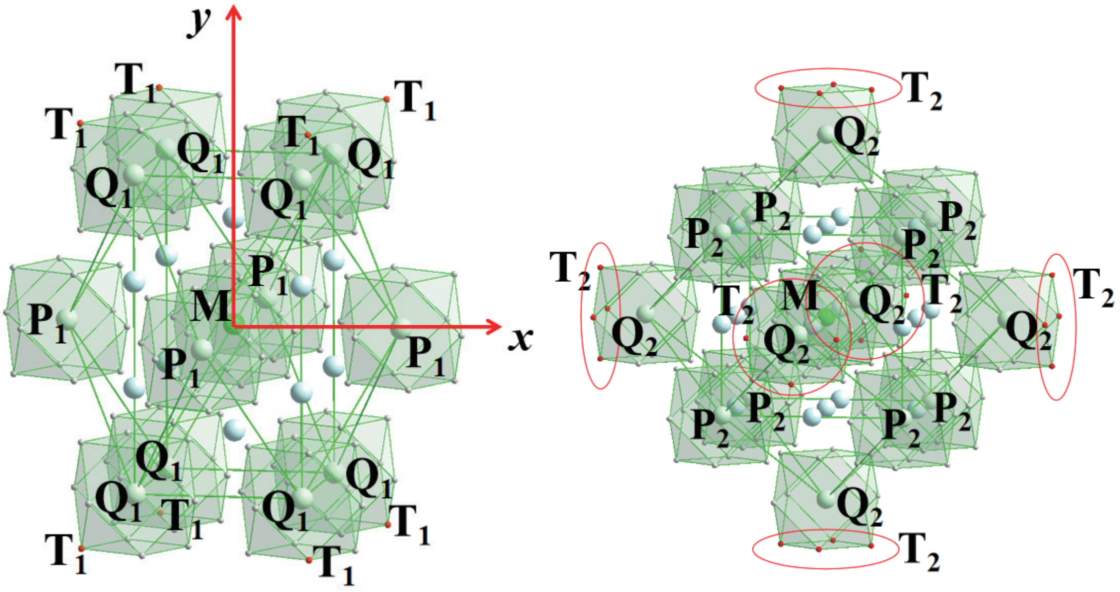

(a) (b)

Fig. 3. (Color online) Alloy cluster models: (a) 1-2 and (b) 1-3 models.

nearest-neighbor clusters around any atom within the model is relatively consistent. Furthermore, the second-shell atoms are evenly separated from the nearest-neighbor clusters. A comparison of the two models shown in Fig. 3(a) reveals that the nearest-neighbor clusters in the 1-2 model are more concentrated along the *X*-axis and less dense along the *Y*-axis. Importantly, in the *Y*-axis direction, two second-shell atoms occupy the cluster gap positions, leading to an overall atomic distribution that is near-uniformity.

Both models can form a supercluster centered on the alloy cluster M with two shell coordination clusters P and Q. Let the position of the central cluster M be denoted as $\langle 0, 0, 0 \rangle$. The outermost atoms T_1 and T_2 in the superclusters of both models are located at positions $\langle \pm 2, \pm 3/2, \pm 1/2 \rangle$ with a distance of $\sqrt{2^2 + (3/2)^2 + (1/2)^2} \times 0.361 = 0.92$ mn units from the center. This distance deviates by approximately 0.13 nm from the position $r = 1.05$ nm, which corresponds to the center of the aforementioned dark ring. The possible sources of this discrepancy are given below.

(1) The theoretical calculation model assumes that the impurity potential is a point-like hard wall potential,(24) whereas the actual adsorption atomic potential field exhibits a gradient distribution, such as D-orbital broadening(24) or chemical bond hybridization.

(2) In calculating the electron potential function, the free electron model is employed,(24) neglecting many-body effects such as electron–electron interactions and electron–phonon coupling in the correction.

(3) STM imaging inherently involves errors. For example, the thermal drift of the sample or needle tip during the experiment may lead to image distortion, with spatial positioning errors ranging from 0.05 to 0.1 nm.

The superclusters formed by the aforementioned neighboring clusters demonstrate significant structural stability and are widely observed in liquid metals. As shown in Ref. 29, liquid EGaln and Galinstan alloys contain minimal medium-range spherical clusters with a diameter of 1.57 nm. Considering that the atomic radii of gallium and indium exceed those of copper, this value closely corresponds to the previously calculated electrically neutral minimum scale. In our prior research,(30) we suggested that the nearest-neighbor cluster, owing to its robust structural integrity, acts as the foundational unit for forming free-standing primary oscillations. The diverse counts of second-nearest-neighbor atoms lead to unique stacking configurations of the nearest-neighbor clusters. More specifically, when the number of atoms in the second shell is either 2 or 3, both the 2-2 and 3-1 models display concurrent sixth-order and fourth-order symmetry axes.

As illustrated in Fig. 4, within the range of r_{cut}, the 2-2 model shows the highest volumetric atomic density, represented as $\rho = \left(\text{Number of atoms in the cutting shell}\right) / r_{cut}^3$. The 3-1 model shows the smallest deviation of r_{cut} from the spherical periodic position and has the second-highest volumetric atomic density following the 2-2 model. As a result, among the 18 cluster stacking models described in Ref. 28, the 2-2 and 3-1 models in Ref. 30 are recognized as the most suitable models for analyzing high-elasticity alloys.

5. Analysis of Chemical Formula of High-elasticity Alloys

Currently, researchers often employ the SRO parameters proposed by Cowley to describe the local chemical order of solute atoms in alloys. The Cowley parameter is defined as $\alpha = 1 - P_A / X_A$, where P_A denotes the actual occupancy probability of A atoms in the coordination shell of B atoms and X_A represents the molar fraction of A atoms within the system. This parameter results

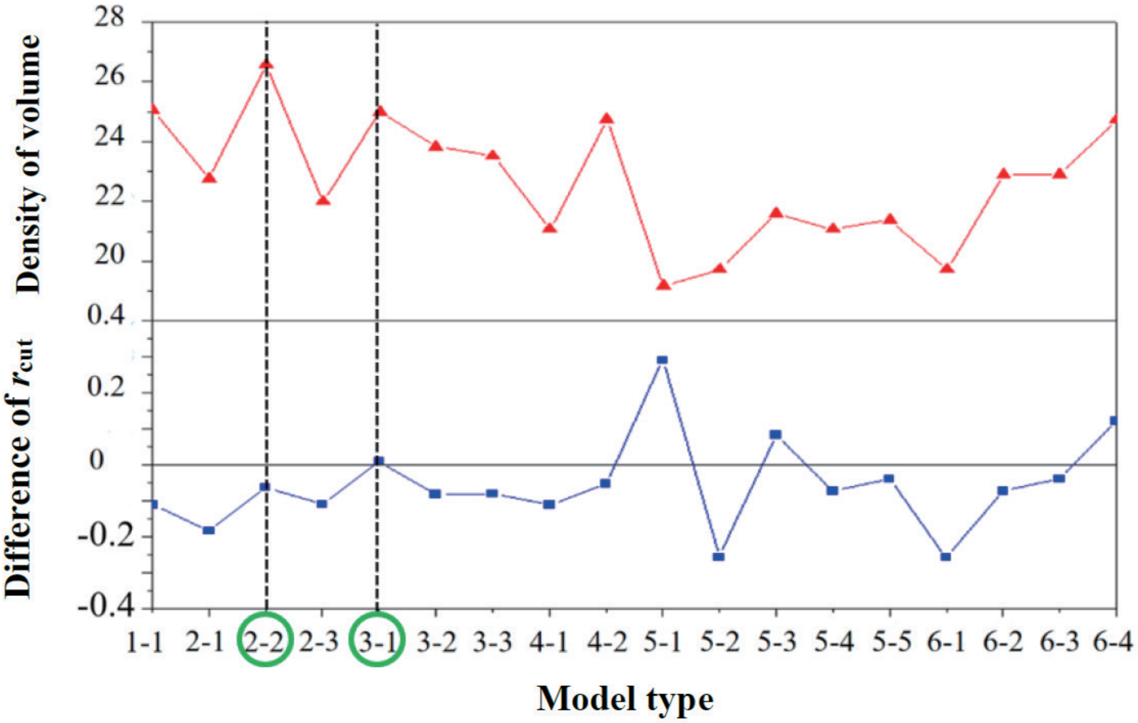

Fig. 4. (Color online) Factors of cutting shell of 18 models proposed in Ref. 29.

from extensive statistical averaging and effectively addresses the issue of atomic occupation across different shells in solid solution alloys.(31,32) Hong *et al.*(26) indicated that the compositions of various binary alloys can be accurately represented by the atomic compositions of the first- and second-nearest-neighbor elements, as calculated using the Cowley parameter, with a deviation of less than 0.1%.

For instance, regarding the highly elastic brass alloy H68 with a primary composition of $Cu_{68}Zn_{32}$, Reinhard *et al.*(33) investigated the quenching equilibrium state of $Cu_{68.9}Zn_{31.1}$ at.% single crystal by elastic diffuse neutron scattering. The ordered parameters for the first- and second-nearest-neighbors were determined as $\alpha_{110} = -0.1373$ and $\alpha_{200} = -0.149$, respectively. By employing the Cowley parameter, the atomic arrangement of the second-nearest-neighbor shell centered on Zn was calculated to be $[Zn–Cu_{9.4}Zn_{2.6}]Cu_{21.76}Zn_{1.24}$, assuming the number of atoms in the second shell to be 3. This formula is referred to as the chemical formula of the alloy. It was found that the chemical composition of the alloy is approximately 30.25%, which aligns closely with its actual composition, exhibiting a deviation of only 0.0085%. This result demonstrates that the two-shell atomic model proposed in this study can effectively be utilized to analyze the composition of highly elastic alloys. For simplicity, the aforementioned chemical formula can be rewritten as $[Zn–Cu_{11.16}Zn_{0.84}]Zn_3$.

Building upon the atomic model and analytical approach for the two nearest coordination shells of highly elastic alloys introduced in this study, Table 1 summarizes the derived chemical compositions of these shells across 13 distinct highly elastic alloy systems. These results provide the basis for several important insights and concluding points.

(1) In Table 1, the number of atoms in the second shell layer of the chemical formula is predominantly either 2 or 3, with the number of atoms in each shell being an integer. For alloys containing small atomic impurities such as Be (e.g., BZn18-26, 3J31, and 3J32), the number of atoms in the second-shell layer consistently equals 2. In contrast, for alloys containing impurities similar in size to the host atoms, the number of atoms in the second-shell layer uniformly equals 3.

(2) If the enthalpy of combination between the added element and the central atom is negative, as shown in Table 2,(34) the added element tends to occupy the first-shell layer. This results in the chemical formula $[A–A_{12-x}B_x]A_3$ or $[A–A_{12-x}B_x]A_2$, where x ranges from 1 to 12. Examples include the copper–titanium alloy QTi4-1, nickel–beryllium alloys 3J31 and 3J32, nickel–chromium alloys Nimonic75 and 3J32, and the iron–nickel alloy 3J1.

(3) If the enthalpy of combination between the added element and the central atom is positive, as shown in Table 2, the added element tends to occupy the second-shell layer. This leads to the chemical formula $[A–A_{12-x}B_x]B_3$ or $[A–A_{12-x}B_x]B_2$, where x ranges from 1 to 12. Examples include brass H68, the copper–tin alloy C52180, the copper–nickel–zinc alloy BZn18-26, and the Monel alloys Monel400, Monel401, and MonelK500.

(4) If the enthalpy of combination between the added element and the central atom is zero, as shown in Table 2, there is no fixed tendency regarding the position of the added element. Its chemical formula is expressed as $[A–A_{12}]A_{3-x}B_x$, where x ranges from 1 to 3. An example is beryllium bronze C17200.

It is important to note that the ideal chemical formula represents the primary chemical composition. By incorporating trace elements based on this primary formula, various real-grade alloys can be obtained. The chemical formula composition reflects a statistical average, indicating a preferential neighborhood relationship among different types of atoms within the two nearest shell layers. This preferential neighborhood relationship refers to the tendency of specific atoms to cluster together in certain configurations, providing a quantitative basis for elucidating the local chemical environment characteristics of the alloy system.

6. Conclusions

To better understand the chemical formula of high-elasticity alloys, we presented the nearest-neighbor two-shell atomic structure model in this work. It was shown that the number of second-shell atoms encircling each central atom is either 2 or 3, which corresponds to the 2-2 and 3-1 models suggested in Ref. 29, depending on the electron oscillation range in the spherical periodic electron resonance model. In both situations, the supercluster model's density peaks inside the spherical period's reduced radius. Moreover, there is a minimal difference between the truncation radius of the spherical period and the actual average truncation radius position of FCC solid solution atoms.

Thirteen exemplary high-elasticity alloys were examined in this study. The mixing enthalpy of impurity elements with host atoms determines where they are placed in the chemical formula. The chemical formulas $[\mathrm{A{-}A}_{12-x}\mathrm{B}_{12}]\mathrm{A}_2$ and $[\mathrm{A{-}A}_{12-x}\mathrm{B}_{12}]\mathrm{A}_3$ are produced when the mixing enthalpy is negative, which causes different atoms to become close neighbors and impurity atoms to tend to occupy the nearest-neighbor shell. In contrast, impurity atoms typically occupy the second-nearest neighbor shell when the mixing enthalpy is positive and comparable atoms are close neighbors, resulting in the chemical formulas $[\mathrm{A{-}A}_{12}]\mathrm{A}_{2-x}\mathrm{B}_x$ and $[\mathrm{A{-}A}_{12}]\mathrm{A}_{3-x}\mathrm{B}_x$. The element locations are left unaltered when the mixing enthalpy is zero. Analysis showed that there is a high degree of consistency between the grade components and the chemical formula components that were derived in this study.

In this study, we introduced an analytical approach that provides substantial theoretical support for the development of new alloys as well as the enhancement of performance in established alloy systems. Additionally, the proposed methodologies enabled the creative design of high-elasticity alloys exhibiting enhanced physical characteristics, which can assist sensor researchers in refining manufacturing processes and promoting the innovation of advanced, high-performance sensing devices.

Acknowledgments

This work was supported in part by the Operational Funding of the Advanced Talents for Scientific Research (Grant no. 19YG04) of Sanming University and the Natural Science Foundation of Sanming University (Grant no. KD23003P). The authors also acknowledge the support from the School of Mechanical and Electric Engineering, Sanming University.

References

1 M. Kaya: Phys. Met. Metall. **126** (2025) 774. https://doi.org/10.1134/S0031918X25601209

2 G. Li, Z. Hang, S. Yue, Q. Liu, Z. Guo, H. Ding, J. Jie, and T. Li: J. Alloys Compd. **946** (2023) 169388. https://doi.org/10.1016/j.jallcom.2023.169388

3 K. He, Y. Chen, H. Lai, and X. Wu: J. Constr. Steel Res. **224** (2025) 109144. https://doi.org/10.1016/j.jcsr.2024.109144

4 Z. Ren, W. Wu, D. Song, and Y. Cheng: AIP Adv. **10** (2020) 105030. https://doi.org/10.1063/5.0026353

5 Z. Liu, L. Zeng, K. Xu, Z. Li, H. Chen, Z. Qiao, Y. Qu, G. Liu, and L. Li: Sensors **22** (2022) 5096. https://doi.org/10.3390/s22145096

6 B. B. Narod and D. M. Miles: Geosci. Instrum. Method. Data Syst. **13** (2024) 131. https://doi.org/10.5194/gi-13-131-2024

7 Y. Shi, C. Guo, X. Xiao, Y. Gong, H. Wang, and B. Yang: J. Alloys Compd. **983** (2024) 173945. https://doi.org/10.1016/j.jallcom.2024.173945

8 L. Wang: J. Mater. Eng. Perform. **31** (2022) 8914. https://doi.org/10.1007/s11665-022-06954-7

9 W. Lin, Q.Y. Lv, D. Jiao, L.B. Zhang, J. Tan, G. Sha, and J. Hu: J. Mater. Sci. Technol. **173** (2024) 31. https://doi.org/10.1016/j.jmst.2023.04.050

10 K. Yang, Y. Wang, M.X. Guo, H. Wang, Y. Mo, X. Dong, and H. Lou: Prog. Mater. Sci. **138** (2023) 101141. https://doi.org/10.1016/j.pmatsci.2023.101141

11 Z. Sun, C. Shi, C. Liu, H. Shi, and J. Zhou: Mater. Des. **223** (2022) 111214. https://doi.org/10.1016/j.matdes.2022.111214

12 S. Ma, J. Zhang, X. Biao, Y. Xiong, S. Wei, and S. Zhao: J. Alloys Compd. **911** (2022) 165144. https://doi.org/10.1016/j.jallcom.2022.165144

13 M. P. Moody, A. V. Ceguerra, A. J. Breen, X. Cui, B. Gault, L. T. Stephenson, R. K. W. Marceau, R. C. Powles, and S. P. Ringer: Nat. Commun. **5** (2014) 5501. https://doi.org/10.1038/ncomms6501

14 W. Sun, Y. Zhu, R. K. W. Marceau, L. Wang, Q. Zhang, X. Gao, and C. Hutchinson: Science **363** (2019) 972. https://doi.org/10.1126/science.aav7086

15 K. Chen, X. Chen, D. Ding, G. Shi, and Z. Wang: Mater. Des. **94** (2016) 338. https://doi.org/10.1016/j.matdes.2016.01.064

16 Q. Zhao and Z. Liu: J. Mater. Sci. **58** (2023) 1. https://doi.org/10.1007/s10853-023-08836-2

17 Z. Li, D. Dong, L. Zhang, S. Zhang, Q. Wang, and C. Dong: Sci. Rep. **12** (2022) 3169. https://doi.org/10.1038/s41598-022-06893-2

18 X. Li, Q. Wang, Y. Sun, S. Sun, and L. Ge: Int. J. Hydrogen Energy **69** (2024) 1341. https://doi.org/10.1016/j.ijhydene.2024.05.162

19 P. Häussler: J. Phys. Colloques **46** (1985) 361. https://doi.org/10.1051/jphyscol:1985854

20 H. Min, E. H. Hwang, and S. D. Sarma: Phys. Rev. B: Condens. Matter. **86** (2012) 081402(R). https://doi.org/10.1103/PhysRevB.86.081402

21 J. Lee, D. Wong, J. Velasco Jr., J. F. Rodriguez-Nieva, S. Kahn, H.-Z. Tsai, T. Taniguchi, K. Watanabe, A. Zettl, F. Wang, L. S. Levitov, and M. F. Crommie: Nat. Phys. **12** (2016) 1032. https://doi.org/10.1038/nphys3805

22 M. Crommie, C. Lutz, and D. M. Eigler: Nature **363** (1993) 524. https://doi.org/10.1038/363524a0

23 J. Kotsakidis, G. M. Stephen, M. DeJarld, R. L. Myers-Ward, K. M. Daniels, D. K. Gaskill, M. S. Fuhrer, R. E. Butera, A. T. Hanbicki, and A. Friedman: ACS Appl. Mater. Interfaces **16** (2024). https://doi.org/10.1021/acsami.4c07724

24 P. Chankowski and J. Wojtkiewicz: Preprint arXiv:2111.14927 (2021). https://doi.org/10.48550/arXiv.2111.14927

25 E. Wahlström, I. Ekvall, H. Olin, and L. Walldén: Appl. Phys. A **66** (1998) S1107. https://doi.org/10.1007/s003390051306

26 H.-L. Hong, C.-H. Yang, H.-X. Yan, and Y.-Y. Lin: Sens. Mater. **36** (2024) 4165. https://doi.org/10.18494/SAM5100

27 M. F. Crommie, C. P. Lutz, and D. M. Eigler: Science **262** (1993) 513. https://doi.org/10.1126/science.262.5131.218

28 H.-L. Hong, C. Dong, Q. Wang, Y. Zhang, and Y. X. Geng: Acta Physica Sinica **65** (2016) 036101. https://doi.org/10.7498/aps.65.036101

29 V. Krishnamurthi, P. H. A. Vaillant, J. Mata, K.-C. Nguyen, G. Bryant, K. Chiang, S. P. Russo, A. J. Christofferson, A. Elbourne, and T. Daeneke: Adv. Mater. **36** (2024) 2403885. https://doi.org/10.1002/adma.202403885

30 H.-L. Hong, C.-H. Yang, H.-X. Yan, L.-H. Zheng, and K.-C. Wang: Sens. Mater. **35** (2023) 4617. https://doi.org/10.18494/SAM4581

31 A. Jarlöv, W.-M. Ji, R. Babicheva, Y. Tian, Z. Hu, H. L. Seet, L. Tan, F. Liu, Y. Liu, M. L. S. Nai, U. Ramamurty, and K. Zhou: Mater. Des. **240** (2024) 112840. https://doi.org/10.1016/j.matdes.2024.112840

32 K. Sheriff, Y. Cao, and R. Freitas: Comput. Mater. **10** (2024) 215. https://doi.org/10.1038/s41524-024-01393-5

33 L. Reinhard, B. Schönfeld, G. Kostorz, and W. Bührer: Phys. Rev. B: Condens. Matter **41** (1990) 1727. https://doi.org/10.1103/PhysRevB.41.1727

34 A. Takeuchi and A. Inoue: Mater. Trans. **46** (2005) 2817. https://doi.org/10.2320/matertrans.46.2817